Solid State Phenomena
ISSN: 1662-9779, Vol. 358, pp 13-21
doi:10.4028/p-sUIIP5

Submitted: 2023-10-02
Revised: 2024-04-18
Accepted: 2024-04-19
Online: 2024-08-21

Coupled Non-Destructive Methods, Kelvin Force Probe Microscopy and µ-Raman to Characterize Doping in 4H-SiC Power Devices

VUILLERMET Enora[1,a], WU Kuan Ting[1,b], SEDILOT Anaël[1,c], DETURCHE Régis[1,d], BERCU Nicolas[2,e], USUREAU Elise[1,f], BEAL Jérémie[1,g] and LAZAR Mihai[1,h *]

[1]Light, nanomaterials & nanotechnologies (L2n), CNRS UMR 7076, University of Technology of Troyes, 12 rue Marie Curie, 10004 Troyes, France

[2]Laboratory of Research in Nanosciences, EA 4682, University of Reims Champagne-Ardenne, Moulin de la Housse, 51100, Reims, France

[a]enora.vuillermet@utt.fr, [b]kuan_ting.wu@utt.fr, [c]anael.sedilot@utt.fr, [d]regis.deturche@utt.fr, [e]nicolas.bercu@univ-reims.fr, [f]elise.usureau@utt.fr, [g]jeremie.beal@utt.fr, [h]mihai.lazar@utt.fr

Keywords: JFET, SiC power devices, devices characterization methods, AFM, KPFM, µ-Raman, SEM

Abstract. Investigation of the doped areas in 4H-SiC power devices has been done by non-destructive characterization methods. It consists of local surface potential measurements by Kelvin Probe Force Microscopy (KPFM) coupled with scanning electron microscopy (SEM) and µ-Raman spectroscopy. Near-field mappings of the devices' surface have been realized, allowing us to discern the differently doped areas.

Introduction

Silicon carbide (SiC) power devices are today mainly employed for high voltage, high frequency, or elevated temperatures applications. The rise of industrial markets, such as the one of electric vehicles, has increased the demand for high-performance power devices, leading to more complex geometry of the components which mostly relies on accurate SiC local doping [1,2]. Therefore, it became necessary now to be able to monitor the doping of SiC devices at all steps of the fabrication process to ensure the planned structure architecture. Accurate doping, controlled at µ-nano scale will guarantee, for example, the effective equipotential distribution in the material and prevent the formation of local and undesired high electrical fields [3]. In this work, the doping in 4H-SiC lateral junction field effect transistors (JFETs) is studied with non-destructive characterization methods like KPFM, µ-Raman, and SEM. Compared to more conventional doping characterization techniques, such as the Hall effect [4] or secondary ion mass spectrometry (SIMS) [5], these methods do not damage the material they are used on and so provide fast and real-time evaluation of local doping profiles with no need for complex samples' preparations. They are thus ideal for monitoring all doping steps of devices even if they are fabricated on large SiC wafers.

Experimental Part

Fabrication of the devices. The analyzed samples in this study are n and p-type lateral junction field effect transistors (JFET). The integrated circuits are conceived on a 4H-SiC wafer commercialized by II-VI COHERENT, with different CVD-grown n and p-type epitaxial layers. Fig. 1 shows a scheme of the JFET structures as well as the depth and doping of the substrate and epitaxial layers. To etch the p-doped layers and separate the n and p-type JFETs, RIE/ICP plasma etching was used. The plasma is composed of SF_6 (25sccm) and O_2 (6.7sccm) gazes [6]. The channels of the transistors were realized by ion implantation of nitrogen (n-doped channel) or aluminum (p-doped channel) in the epitaxial layers. Second ion implantation of nitrogen (or aluminum) was performed to conceive the n^+-doped (or p^+-doped) sources, drains, and gates. Table 1 summarizes the different ion implantations realized [7]. Activation of the dopants was done by annealing at 1650°C for 45 minutes,

under argon, of the samples. Finally, the metallization of the JFETs has been done. The structures of the ohmic contacts were Ti/Ni for n-doped 4H-SiC and Ni/Ti/Al/Ni for p-doped 4H-SiC and were respectively annealed at 900 and 800°C for 90 seconds [8].

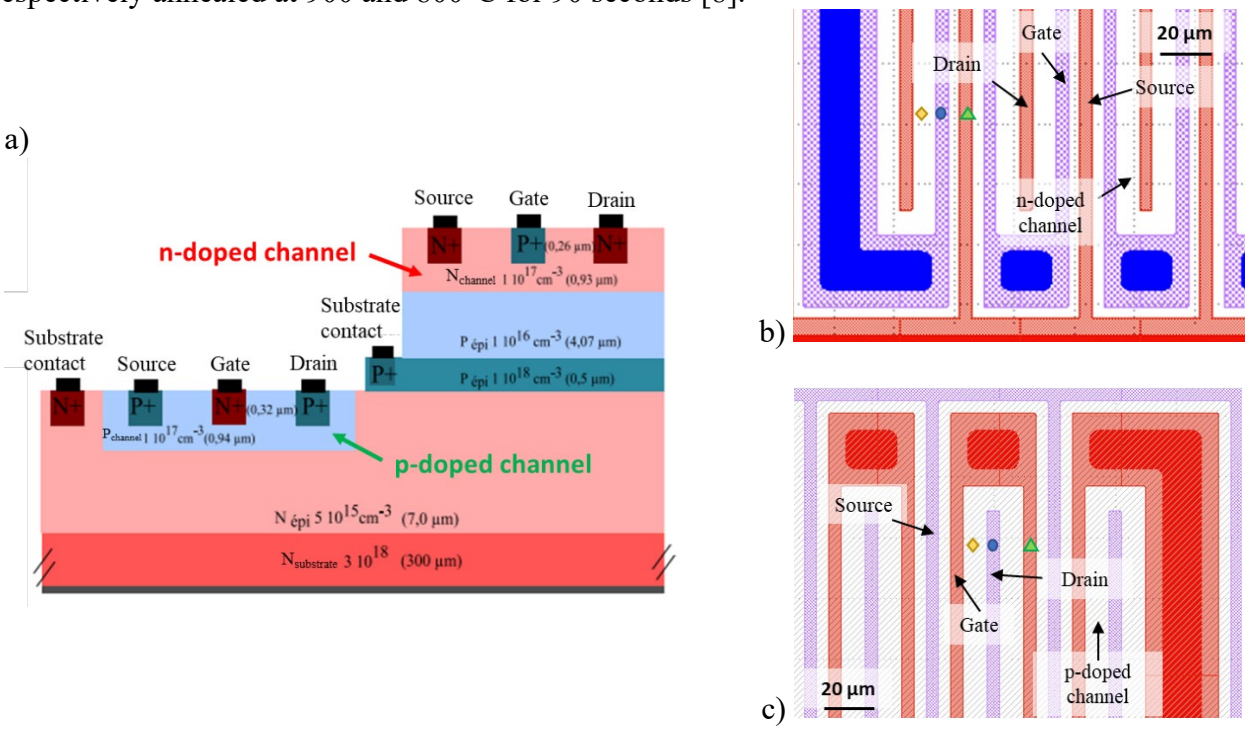

Fig. 1. Vertical scheme of the JFETs structures (a) and top view of n-type (b) and p-type (c) JFETs. Green triangles, blue circles, and yellow lozenges correspond to n^+-doping, p^+-doping, and the doped channels of the JFETs respectively. Blue and red plots in (b) and (c) images are the metallic contacts.

Table 1. Description of the ion implantations performed in the JFETs

Samples		Type	Doping [cm^{-3}]	Depth [µm]
n-type JFET	Channel	n	2×10^{17}	0.93
	Source and Drain	n^+	3×10^{19}	0.32
	Gate	p^+	3×10^{19}	0.26
p-type JFET	Channel	p	2×10^{17}	0.94
	Source and Drain	p^+	3×10^{19}	0.26
	Gate	n^+	3×10^{19}	0.32

Characterization methods. Non-destructive characterization methods were used to analyze the samples. Because n^+ and p^+-type doping were achieved through ion implantation at the surface of the samples (depth of less than 1µm), a Hitachi SU-8030 FEG-SEM (field emission gun-scanning electron microscope) was used in secondary electrons mode to detect the differently doped areas at the surface.

Additionally, these areas were identified using a LabRAM HR Evolution Raman microscope from Horiba with a UV laser line (325nm). The µRaman measurements have been performed under a backscattered geometric configuration excited at room temperature (RT). To carry out the measurements, a 40× long-focus objective lens and a 100 µm confocal pinhole were used with a grating of 1800g/mm. Raman spectroscopy depends on the discrete vibrational states of the SiC atoms (phonons). The spectra obtained are thus directly associated with the crystallography of the material [9]. The low excitation wavelength ensures that the laser remains confined to the device's surface [10,11].

Kelvin probe force microscopy (KPFM) is an electrical mode of atomic force microscopy (AFM). In this work, the Dimension Icon AFM from Bruker is employed in peak force frequency modulated mode (FM-KPFM) [12], along with SCM-PIT V2 tips. First, the tip scans the surface in Peak Force

Tapping mode to measure its topography. Then, the tip is lifted to measure the surface potential. In FM-KPFM mode, a modulation signal (AC) is applied to the cantilever to vibrate it at its resonance frequency. Simultaneously, a bias voltage (DC) is applied between the tip and the sample, inducing electrostatic forces between the two. These forces generate a dephasing of the cantilever's resonance frequency, and the DC voltage is adjusted to offset this dephasing and nullify the impact of the induced electrostatic forces. The DC signal is thus equal to the tip-sample contact potential difference (CPD), representing the difference in work functions between the tip and the sample. Fluctuations in the DC signal lead to the surface potential mapping of the samples [13,14].

Results

Fig. 2.a and 2.b respectively show the surface of the n-type and p-type JFETs. While the metallization of the devices is easily observed under microscope imaging, the successive n^+ and p^+ type doping inside the channels are not visible at all. However, under SEM observation, the various types of doping can be distinguished (Fig. 2.c.d). The symbols found on the different images can be associated with the channel (lozenges), n^+ (triangles), and p^+ (circles) doping of the JFETs. In the SEM images, the n^+-doping appears darker than the n or p-doped channels whereas the p^+ doping appears lighter. This suggests that fewer secondary electrons are collected from n^+-doping compared to p^+ doping. It also appears that the thicknesses of the n^+ and p^+-doped areas are larger than expected (Fig. 1.b.c). This could be attributed to a masking issue during the ion implantation process. The p or n-doped channels are thus very thin at the surface of the samples, making them more difficult to observe.

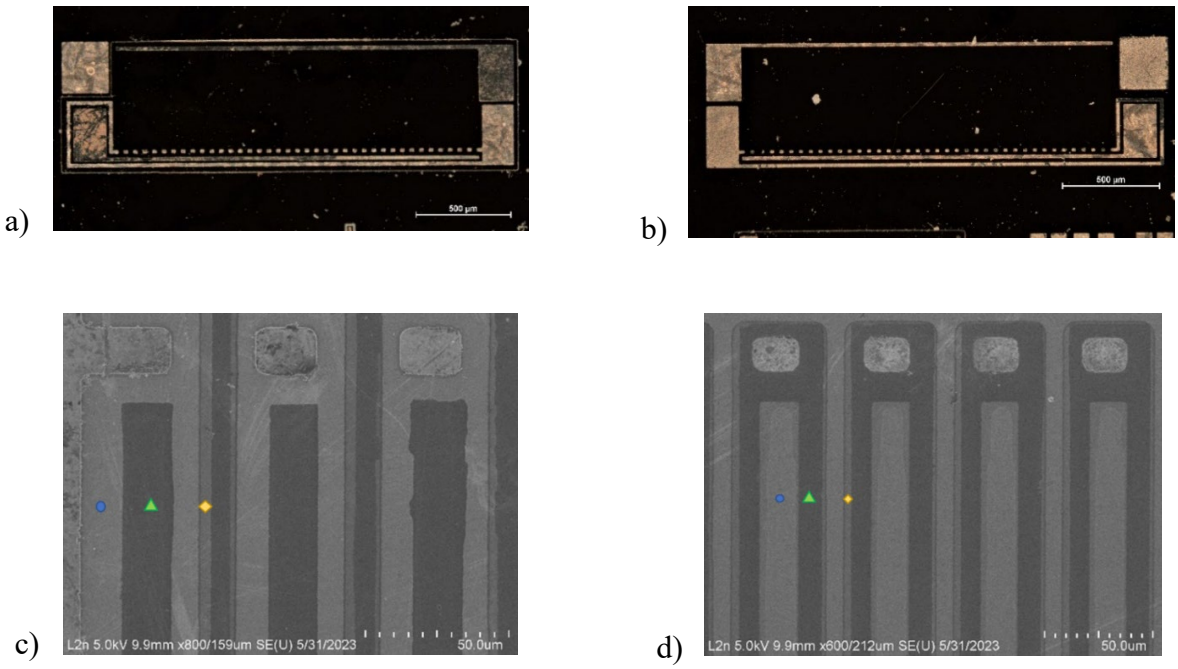

Fig. 2. Darkfield microscope images (obj x5) of n-type (a) and p-type (b) JFETs. (c) and (d) are the SEM images of the n-type and p-type JFETs respectively

Fig. 3 illustrates the surface potential mappings of the JFETs, which corresponds to the difference in work functions between the AFM tip and the sample. The surface potential fluctuations coincide with the variations in the number of secondary electrons detected by the SEM, confirming the issue of the too large n^+ and p^+-doped areas, reducing the thickness of the JFETs channels at the sample's surface. This time, the p^+-doping displays a higher potential (~250mV) than the n^+-doping (~ -350mV). However, the n-doped channel presents a surface potential value that falls between the values of n^+ and p^+-doping (~100mV), while the p-doped channel presents a surface potential that surpasses both, n^+ and p^+-doping (370mV).

The Raman measurements reveal the spectra of the different doping present in the 4H-SiC JFETs (Fig. 4.a). Distinctive peaks characteristic of 4H-SiC are found. Fig. 4.c. and 4.d show the Raman spectra of the different doping in the n-type JFET. The intensity of the LO peak is slightly reduced for the n^+ doping compared to the p^+ one. Raman mappings of the JFETs coincide with the KPFM mappings. In both JFETs, the LO peak is lower in intensity for n^+ doping than for p^+ doping. The demarcation between the differently doped areas is more easily discernible in the p-type JFET compared to the n-type JFET.

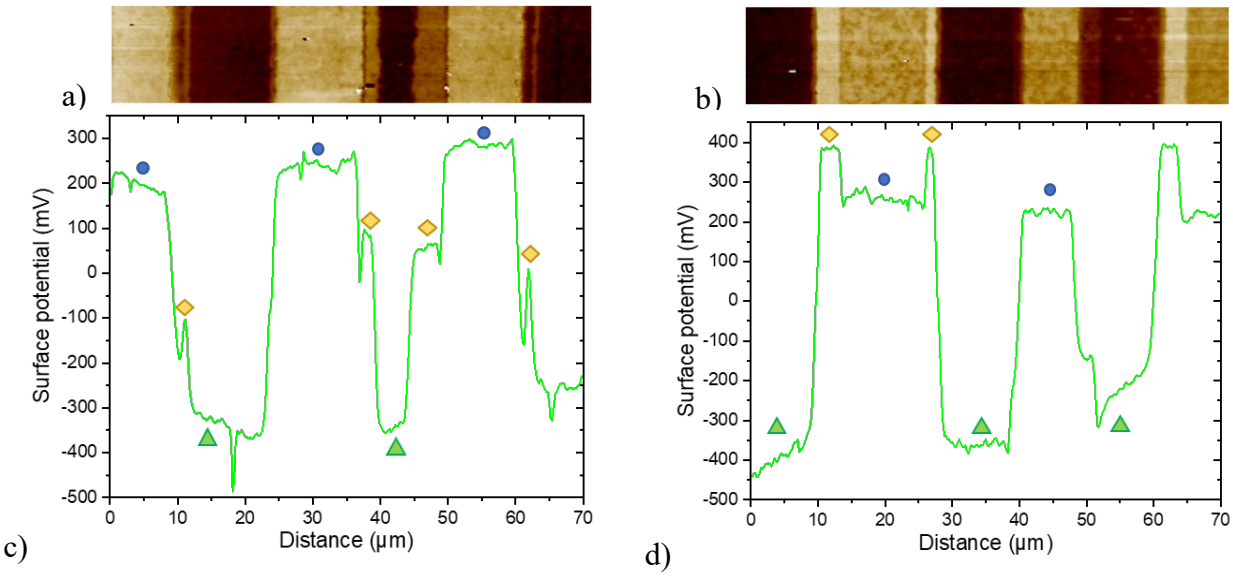

Fig.3. n and p-type JFETs respective KPFM mappings (a), (b) and measured surface potential (c), (d)

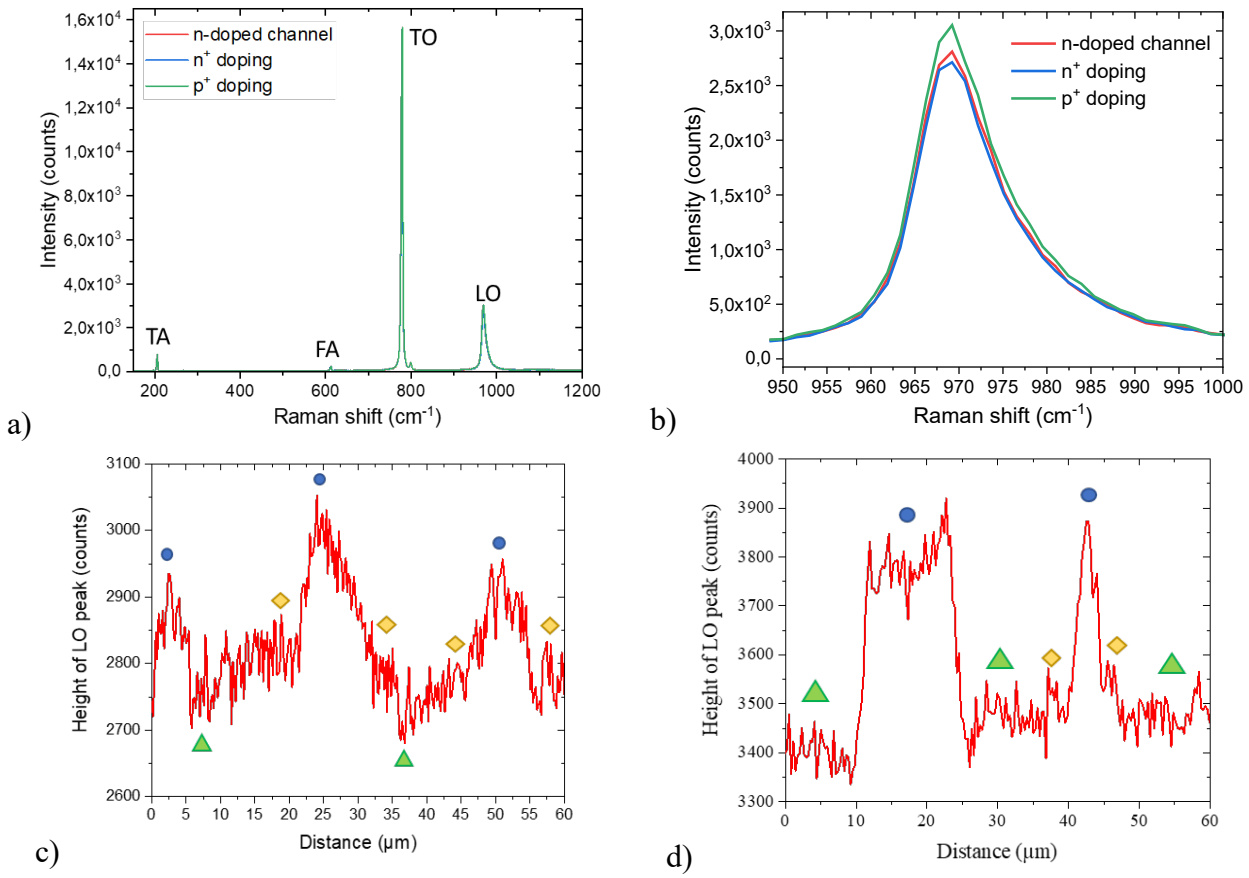

Fig. 4. (a) Raman spectra of the doped areas of the n-type JFET. (b) Zoom in the LO peak. (c) and (d) are respectively the Raman mappings of the n-type and p-type JFETs

Discussion

For SEM measurements, the variation in the contrast between the n and p-doped areas is not attributed to a difference in surface topography but comes from the dissimilar doping charges present in the two zones. Indeed, the p-n junctions present in the JFETs form an electric field that drives away electrons from the p-doped region and attracts them near the n-doped region. The built-in potential for p-n junctions and isotype homo-junctions can be measured with the formulas (1) and (2) respectively [15].

$$V_{pn} = \frac{kT}{q} \ln \frac{N_A N_D}{n_i^2} \quad (1)$$

$$V_{iso} = \frac{kT}{q} \ln \frac{N^1}{N^2} \quad (2)$$

With N_A and N_D the respective concentrations of acceptors and donors, N^1 and N^2 respectively the higher and lower doping concentrations, n_i the intrinsic carrier density, k the Boltzmann constant, T the temperature in degrees Kelvin, and q the elementary charge.

Because this electrical potential possesses generally a low strength, it affects SEM imaging only when the emitted secondary electrons from the material have a low energy. The electric field causes the acceleration of the electrons emitted from the p-doped areas and the deceleration of the electrons emitted from the n-doped ones. The built-in potential also manifests in isotype homo-junctions but with a lower force compared to p-n junctions. That phenomenon explains why, at the JFETs' surface, the p^+ doping appears brighter than the n^+ one. When comparing two n-type (p-type) doping, the one with a greater number of donors (acceptors) appears darker (lighter) in SEM imaging [15,16].

KPFM measures the contact potential difference (CPD) between the AFM tip and the sample's surface which corresponds to their difference in work function. So, the CPD depends on the Fermi level of the material and can be expressed by the formulas (3) and (4) for p and n-doping respectively [14].

$$V_{CPD}^{p} = \frac{1}{q}\left(\chi + \frac{E_g}{2} + k_B T. \ln\left(\frac{N_A}{n_i}\right) - \Phi_m\right) \quad (3)$$

$$V_{CPD}^{n} = \frac{1}{q}\left(\chi + \frac{E_g}{2} - k_B T. \ln\left(\frac{N_D}{n_i}\right) - \Phi_m\right) \quad (4)$$

With q the elementary charge, χ the electron affinity, E_g the band gap, k_B the Boltzmann constant, T the temperature, Φ_m the work function of the metallic tip, N_A, N_D, and n_i the respective acceptor, donor, and intrinsic carrier densities.

In semiconductors, n-type doping leads to an increase in the Fermi level due to electrons accumulation whereas p-type doping leads to the opposite due to holes' accumulation. So, in 4H-SiC, p-doping should present a higher CPD than n-doping [14]. Moreover, according to formulas (3) and (4), the CPD should increase when the concentration of aluminum introduced in SiC for p-type doping increases. The opposite should occur for n-type doping. However, interface charge states, defect states in the SiC bandgap, or surface defects can influence the Fermi level, leading to band bending and fluctuations in the CPD value which are not taken into account in the preceding formulas. In extreme cases, the CPD value can even be pinned and become independent from the Fermi level [14,17,18]. In this work, for both n (Fig. 3.c) and p-type (Fig. 3.d) JFETs, the p^+-doped areas have a higher surface potential than the n^+-doped ones which follows the theory. However, for the p-type JFET, the surface potential of the p-doped channel is higher than the one of the p^+-doped wells whereas a reduction in hole concentration should decrease the value of the CPD measured. In the case of the n-type JFET, the surface potential of the n-doped channel is between the ones of n^+ and p^+ doping, which respects the theory. But, the potential value of the n-doped channel (~100mV) is closer to the potential of p^+-doped wells (~250mV) than to the potential of n^+-doped wells (~ -350mV). The CPD values of the p

and n-doped channels are reproducible and occur at each KPFM measurement, at different locations of the JFETs' surface so it is unlikely that their elevated values of surface potential are due to local surface defects.

On the other hand, defect states in the band gap of 4H-SiC can result in downward band bending for p-type doping and upward band bending for n-type doping at the surface of the sample [14,18]. In this work, the first ion implantation of nitrogen or aluminum realized the n or p-doped channels of the JFETs. A second one was then performed to create the n^+ and p^+-doped wells. However, ion implantation is known to generate defect states and lattice damage in SiC, especially for implantations of high concentrations of dopants [19,20]. The induced damage in 4H-SiC can be mostly healed by high-temperature annealing but residual defects will be still present within the material. Moreover, high-temperature annealing can also generate deep-level traps, also called compensating defects, which reduce the free carrier density in the implanted material, especially for Al-doped layers [19–21]. So, it is possible that these compensating defects appeared in the p^+-doped wells of the JFETs generated by ion implantation of high concentrations of aluminum. The presence of these defects could cause downward band-bending and a drop in surface potential for the p^+-doped wells of the JFETs [14,17,18]. That would explain why the surface potential of the p-doped channel is above the one of the p^+-doping in the p-type JFET and why the surface potential of the n-doped channel is close to the one of the p^+-doping in the n-type JFET. Laser illumination of the samples can be used to offset this phenomenon of band bending due to the diffusion of photon-induced electron-hole pairs towards the surface [17].

For μ-Raman measurements, the Raman spectra of the different doped areas (Fig. 4.a) show the typical peaks of 4H-SiC with good crystallinity [9,22,23]. In this work, we are interested in the changes in the shape of the LO peak of 4H-SiC. Indeed, the doping of SiC is well known to affect the shape and position of the Raman peak associated with the longitudinal optical (LO) phonon. An increase in doping concentration leads generally to a decrease in the intensity of the LO peak and an increase in its width [24–26]. When nitrogen (n-type doping) or aluminum (p-type doping) atoms are introduced in SiC, they can deform its lattice due to the difference in size between the dopant species and the silicon or carbon atoms. The induced stress in the lattice can then lead to a shift in the phonon oscillation frequency and so a shift in the position of the LO peak [10,24]. Furthermore, nitrogen and aluminum doping respectively bring free electrons and holes in the SiC crystalline structure. The shape and position of the Raman LO peak can also be affected by the coupling between the LO phonon and the plasmons induced by the collective oscillations of the free charges under laser excitation [9,24]. However, the phonons are more easily coupled with free electrons than holes at room temperature [24,26–28] due to the weak mobility of holes within 4H-SiC [3]. So, for Al-doped SiC, the position, and shape of the LO peak will be mainly dependent on the deformation of the lattice due to the size of aluminum compared to silicon whereas, for n-doped SiC, it will be more dependent on the LO-phonon-plasmon coupling.

Generally, for the same concentration of dopants, n-type doping tends to lower the intensity of the LO peak more than p-type doping [24,29]. This trend is confirmed in Fig. 4.c.d where, for both JFETs, the height of the LO peak is lower for n^+ doping than p^+ doping. Moreover, for the same dopant species, the intensity of the LO peak is supposed to decrease with the dopant concentration [26,27,30]. Consequently, in the n-type JFET, the n-doped channel presents a LO peak with a higher intensity than the n^+-doping. However, for the p-type JFET, the p-doped channel presents a lower intensity for the LO peak than the p+-doped areas. Moreover, with a 100-fold difference in dopant concentration, the variation in the intensity of the LO peak is supposed to be more important than what is shown in Fig. 4.b [24,28,30]. This can be due to the fact that, even with the use of a laser line at a low wavelength (325nm), the laser beam still penetrates a few micrometers deeper in the material [10,31]. So, added to the photons emission of the p^+ and n^+ doping, photons emitted by the n-doped (p-doped) channel and the p-doped (n-doped) epilayer situated below can be detected which disturb the analysis of the results. Moreover, point defects in the SiC lattice can also affect the shape of the LO peak and

lower its intensity. They could have been induced during ion implantation of the JFETs, even if after annealing at 1650°C for 45 minutes, most of them should have been healed [32,33].

Conclusion

Non-destructive SEM, KPFM, and μ-Raman characterization methods are a powerful way to identify doped and functional junctions in electronic devices such as JFETs. The different mappings of the device surface allow us to find the location of the different doped areas. It is also possible to monitor the presence of high electric fields at the surface of the device structures with KPFM. However, KPFM and μ-Raman measurements are also dependent on other physical phenomena. Indeed, the surface potential obtained by KPFM is impacted by surface defects and the charges present in the material. In the case of μ-Raman, the height of the LO peak is also dependent on the defects inherent to the material or created during the ion implantation doping process. For the investigation of thin layers, there is also the question of the too-high laser diffusion depth in the material. These methods are thus ideal for fast and qualitative monitoring of the doping profiles, allowing us to discern an issue with the masking of the sample during the ion implantation or the selective etching of the multi-epitaxial layer process.

Acknowledgments

The authors also acknowledge the use of resources from the NanoPHOT graduate school, the Nanomat platform, part of the Renatech platform, supported by the Ministère de l'Enseignement Supérieur et de la Recherche, the Région Grand Est, and FEDER funds from the European Community.

References

[1] W. Cao, S. Ying, X. Ge, D. Liu, SiC Superjunction MOSFET with Schottky diode for improving short-circuit and reverse recovery Ruggedness, Micro and Nanostructures (2024) 207847. https://doi.org/10.1016/j.micrna.2024.207847.

[2] B. Shi, A.I. Ramones, Y. Liu, H. Wang, Y. Li, S. Pischinger, J. Andert, A review of silicon carbide MOSFETs in electrified vehicles: Application, challenges, and future development, IET Power Electronics 16 (2023) 2103–2120. https://doi.org/10.1049/pel2.12524.

[3] J. Camassel, S. Contreras, Matériaux semiconducteurs à grand gap : le carbure de silicium (SiC), Électronique (2012). https://doi.org/10.51257/a-v2-e1990.

[4] W.C. Mitchel, W.D. Mitchell, M.E. Zvanut, G. Landis, High temperature Hall effect measurements of semi-insulating 4H–SiC substrates, Solid-State Electronics 48 (2004) 1693–1697. https://doi.org/10.1016/j.sse.2004.02.025.

[5] M.A. Pinault-Thaury, F. Jomard, Nitrogen Investigation by SIMS in Two Wide Band-Gap Semiconductors: Diamond and Silicon Carbide, Materials Science Forum 1062 (2022) 376–382. https://doi.org/10.4028/p-684nsi.

[6] M. Lazar, F. Enoch, F. Laariedh, D. Planson, P. Brosselard, Influence of the Masking Material and Geometry on the 4H-SiC RIE Etched Surface State, Materials Science Forum 679–680 (2011) 477–480. https://doi.org/10.4028/www.scientific.net/MSF.679-680.477.

[7] M. Lazar, F. Laariedh, P. Cremillieu, D. Planson, J.-L. Leclercq, The channeling effect of Al and N ion implantation in 4H–SiC during JFET integrated device processing, Nuclear Instruments and Methods in Physics Research Section B: Beam Interactions with Materials and Atoms 365 (2015) 256–259. https://doi.org/10.1016/j.nimb.2015.07.033.

[8] F. Laariedh, M. Lazar, P. Cremillieu, J. Penuelas, J.-L. Leclercq, D. Planson, The role of nickel and titanium in the formation of ohmic contacts on p-type 4H–SiC, Semicond. Sci. Technol. 28 (2013) 045007. https://doi.org/10.1088/0268-1242/28/4/045007.

[9] S. Nakashima, H. Harima, Raman Investigation of SiC Polytypes, Physica Status Solidi (a) 162 (1997) 39–64. https://doi.org/10.1002/1521-396X(199707)162:1<39::AID-PSSA39>3.0.CO;2-L.

[10] Z. Xu, Z. He, Y. Song, X. Fu, M. Rommel, X. Luo, A. Hartmaier, J. Zhang, F. Fang, Topic Review: Application of Raman Spectroscopy Characterization in Micro/Nano-Machining, Micromachines 9 (2018) 361. https://doi.org/10.3390/mi9070361.

[11] Y. Song, Z. Xu, T. Liu, M. Rommel, H. Wang, Y. Wang, F. Fang, Depth Profiling of Ion-Implanted 4H–SiC Using Confocal Raman Spectroscopy, Crystals 10 (2020) 131. https://doi.org/10.3390/cryst10020131.

[12] Kelvin Probe Force Microscopy (KPFM), (n.d.). https://www.bruker.com/en/products-and-solutions/microscopes/materials-afm/afm-modes/kpfm.html (accessed September 14, 2023).

[13] N. Bercu, M. Lazar, O. Simonetti, P.M. Adam, M. Brouillard, L. Giraudet, KPFM - Raman Spectroscopy Coupled Technique for the Characterization of Wide Bandgap Semiconductor Devices, MSF 1062 (2022) 330–334. https://doi.org/10.4028/p-c35702.

[14] U. Gysin, E. Meyer, Th. Glatzel, G. Günzburger, H.R. Rossmann, T.A. Jung, S. Reshanov, A. Schöner, H. Bartolf, Dopant imaging of power semiconductor device cross sections, Microelectronic Engineering 160 (2016) 18–21. https://doi.org/10.1016/j.mee.2016.02.056.

[15] M. Buzzo, M. Ciappa, W. Fichtner, Imaging and dopant profiling of silicon carbide devices by secondary electron dopant contrast, IEEE Transactions on Device and Materials Reliability 6 (2006) 203–212. https://doi.org/10.1109/TDMR.2006.876605.

[16] S. Chung, V. Wheeler, R. Myers-Ward, L.O. Nyakiti, C.R. Eddy, D.K. Gaskill, M. Skowronski, Y.N. Picard, Secondary electron dopant contrast imaging of compound semiconductor junctions, Journal of Applied Physics 110 (2011) 014902. https://doi.org/10.1063/1.3597785.

[17] H. Rossmann, U. Gysin, A. Bubendorf, T. Glatzel, S.A. Reshanov, A. Schöner, T.A. Jung, E. Meyer, H. Bartolf, Two-Dimensional Carrier Profiling on Lightly Doped n-Type 4H-SiC Epitaxially Grown Layers, Materials Science Forum 821–823 (2015) 269–272. https://doi.org/10.4028/www.scientific.net/MSF.821-823.269.

[18] Th. Glatzel, S. Sadewasser, R. Shikler, Y. Rosenwaks, M.Ch. Lux-Steiner, Kelvin probe force microscopy on III–V semiconductors: the effect of surface defects on the local work function, Materials Science and Engineering: B 102 (2003) 138–142. https://doi.org/10.1016/S0921-5107(03)00020-5.

[19] F. Roccaforte, F. Giannazzo, G. Greco, Ion Implantation Doping in Silicon Carbide and Gallium Nitride Electronic Devices, Micro 2 (2022) 23–53. https://doi.org/10.3390/micro2010002.

[20] Y.-D. Tang, X.-Y. Liu, Z.-D. Zhou, Y. Bai, C.-Z. Li, Defects and electrical properties in Al-implanted 4H-SiC after activation annealing*, Chinese Phys. B 28 (2019) 106101. https://doi.org/10.1088/1674-1056/ab3cc2.

[21] J. Weise, C. Csato, M. Hauck, J. Erlekampf, S. Akhmadaliev, M. Rommel, H. Mitlehner, M. Rub, M. Krieger, A. Bauer, V. Haublein, T. Erlbacher, L. Frey, Impact of Al-Ion Implantation on the Formation of Deep Defects in n-Type 4H-SiC, 2018 22nd International Conference on Ion Implantation Technology (IIT) (2018) 66–69. https://doi.org/10.1109/IIT.2018.8807980.

[22] J.C. Burton, L. Sun, F.H. Long, Z.C. Feng, I.T. Ferguson, First- and second-order Raman scattering from semi-insulating 4H-SiC, (n.d.) 3.

[23] X. Qin, X. Li, X. Chen, X. Yang, F. Zhang, X. Xu, X. Hu, Y. Peng, P. Yu, Raman scattering study on phonon anisotropic properties of SiC, Journal of Alloys and Compounds 776 (2019) 1048–1055. https://doi.org/10.1016/j.jallcom.2018.10.324.

[24] X.-B. Li, Z.-Z. Chen, E.-W. Shi, Effect of doping on the Raman scattering of 6H-SiC crystals, Physica B: Condensed Matter 405 (2010) 2423–2426. https://doi.org/10.1016/j.physb.2010.02.058.

[25] H. Harima, S. Nakashima, T. Uemura, Raman scattering from anisotropic LO-phonon–plasmon–coupled mode in *n* -type 4H– and 6H–SiC, Journal of Applied Physics 78 (1995) 1996–2005. https://doi.org/10.1063/1.360174.

[26] T. Mitani, S. Nakashima, M. Tomobe, S. Ji, K. Kojima, H. Okumura, Carrier Density Dependence of Fano Type Interference in Raman Spectra of p-type 4H-SiC, Materials Science Forum 778–780 (2014) 475–478. https://doi.org/10.4028/www.scientific.net/MSF.778-780.475.

[27] H. Harima, T. Hosoda, S. Nakashima, Carrier Density Evaluation in P-Type SiC by Raman Scattering, MSF 338–342 (2000) 607–610. https://doi.org/10.4028/www.scientific.net/MSF.338-342.607.

[28] P. Kwasnicki, R. Arvinte, H. Peyre, M. Zielinski, L. Konczewicz, S. Contreras, J. Camassel, S. Juillaguet, Raman Investigation of Heavily Al Doped 4H-SiC Layers Grown by CVD, Materials Science Forum 806 (2015) 51–55. https://doi.org/10.4028/www.scientific.net/MSF.806.51.

[29] S. Lin, Z. Chen, L. Li, C. Yang, Effect of impurities on the Raman scattering of 6H-SiC crystals, Mat. Res. 15 (2012) 833–836. https://doi.org/10.1590/S1516-14392012005000108.

[30] S. Nakashima, T. Kitamura, T. Mitani, H. Okumura, M. Katsuno, N. Ohtani, Raman scattering study of carrier-transport and phonon properties of 4 H − Si C crystals with graded doping, Phys. Rev. B 76 (2007) 245208. https://doi.org/10.1103/PhysRevB.76.245208.

[31] H. Harima, Raman scattering characterization on SiC, Microelectronic Engineering 83 (2006) 126–129. https://doi.org/10.1016/j.mee.2005.10.037.

[32] K. Piskorski, M. Guziewicz, M. Wzorek, L. Dobrzański, Investigation of Al- and N-implanted 4H–SiC applying visible and deep UV Raman scattering spectroscopy, AIP Advances 10 (2020) 055315. https://doi.org/10.1063/1.5144579.

[33] K. Kamalakkannan, R. Rajaraman, B. Sundaravel, G. Amarendra, K. Sivaji, Raman studies in Al+ implanted semi insulating 6H-SiC, Materials Letters 344 (2023) 134404. https://doi.org/10.1016/j.matlet.2023.134404.